Compact and portable low-coherence interferometer with off-axis geometry for quantitative phase microscopy and nanoscopy

Pinhas Girshovitz* **and Natan T. Shaked**

Department of Biomedical Engineering, Faculty of Engineering, Tel Aviv University, Tel Aviv 69978, Israel
**pinhasgi@tau.ac.il*

Abstract: We present a simple-to-align, highly-portable interferometer, which is able to capture wide-field, off-axis interference patterns from transparent samples under low-coherence illumination. This small-dimensions and low-cost device can be connected to the output of a transmission microscope illuminated by a low-coherence source and measure sub-nanometric optical thickness changes in a label-free manner. In contrast to our previously published design, the τ interferometer, the new design is able to fully operate in an off-axis holographic geometry, where the interference fringes have high spatial frequency, and the interference area is limited only by the coherence length of the source, and thus it enables to easily obtain high-quality quantitative images of static and dynamic samples. We present several applications for the new design including nondestructive optical testing of transparent microscopic elements with nanometric thickness and live-cell imaging.

OCIS codes: (070.2615) Frequency filtering; (090.1995) Digital holography; (090.2880) Holographic interferometry; (110.0180) Microscopy; (180.3170) Interference microscopy.

References and links

1. G. Popescu, T. Ikeda, C. A. Best, K. Badizadegan, R. R. Dasari, and M. S. Feld, "Erythrocyte structure and dynamics quantified by Hilbert phase microscopy," J. Biomed. Opt. **10**(6), 060503 (2005).
2. B. Rappaz, A. Barbul, Y. Emery, R. Korenstein, C. Depeursinge, P. J. Magistretti, and P. Marquet, "Comparative study of human erythrocytes by digital holographic microscopy, confocal microscopy, and impedance volume analyzer," Cytometry A **73A**(10), 895–903 (2008).
3. B. Kemper, A. Bauwens, A. Vollmer, S. Ketelhut, P. Langehanenberg, J. Müthing, H. Karch, and G. von Bally, "Label-free quantitative cell division monitoring of endothelial cells by digital holographic microscopy," J. Biomed. Opt. **15**(3), 036009 (2010).
4. N. T. Shaked, L. L. Satterwhite, M. J. Telen, G. A. Truskey, and A. Wax, "Quantitative microscopy and nanoscopy of sickle red blood cells performed by wide field digital interferometry," J. Biomed. Opt. **16**(3), 030506 (2011).
5. P. Girshovitz and N. T. Shaked, "Generalized cell morphological parameters based on interferometric phase microscopy and their application to cell life cycle characterization," Biomed. Opt. Express **3**(8), 1757–1773 (2012).
6. S. Gawad, M. Giugliano, M. Heuschkel, B. Wessling, H. Markram, U. Schnakenberg, P. Renaud, and H. Morgan, "Substrate arrays of iridium oxide microelectrodes for in vitro neuronal interfacing," Front Neuroeng **2**, 1–7 (2009).
7. M. C. Potcoava and M. K. Kim, "Fingerprint biometry applications of digital holography and low-coherence interferography," Appl. Opt. **48**(34), H9–H15 (2009).
8. V. Mico, Z. Zalevsky, and J. García, "Common-path phase-shifting digital holographic microscopy: a way to quantitative phase imaging and superresolution," Opt. Commun. **281**(17), 4273–4281 (2008).
9. V. Micó and J. García, "Common-path phase-shifting lensless holographic microscopy," Opt. Lett. **35**(23), 3919–3921 (2010).
10. P. Bon, G. Maucort, B. Wattellier, and S. Monneret, "Quadriwave lateral shearing interferometry for quantitative phase microscopy of living cells," Opt. Express **17**(15), 13080–13094 (2009).
11. M. Lee, O. Yaglidere, and A. Ozcan, "Field-portable reflection and transmission microscopy based on lensless holography," Biomed. Opt. Express **2**(9), 2721–2730 (2011).
12. R. Chmelík and Z. Harna, "Parallel-mode confocal microscope," Opt. Eng. **38**(10), 1635–1639 (1999).

#178929 - $15.00 USD Received 1 Nov 2012; revised 24 Dec 2012; accepted 1 Jan 2013; published 1 Mar 2013

13. P. Kolman and R. Chmelík, "Coherence-controlled holographic microscope," Opt. Express **18**(21), 21990–22003 (2010).
14. Z. Monemhaghdoust, F. Montfort, Y. Emery, C. Depeursinge, and C. Moser, "Dual wavelength full field imaging in low coherence digital holographic microscopy," Opt. Express **19**(24), 24005–24022 (2011).
15. Z. Wang, L. J. Millet, M. Mir, H. Ding, S. Unarunotai, J. A. Rogers, M. U. Gillette, and G. Popescu, "Spatial light interference microscopy (SLIM)," Opt. Express **19**(2), 1016–1026 (2011).
16. B. Bhaduri, H. Pham, M. Mir, and G. Popescu, "Diffraction phase microscopy with white light," Opt. Lett. **37**(6), 1094–1096 (2012).
17. N. T. Shaked, Y. Zhu, N. Badie, N. Bursac, and A. Wax, "Reflective interferometric chamber for quantitative phase imaging of biological sample dynamics," J. Biomed. Opt. **15**(3), 030503 (2010).
18. J. Jang, C. Y. Bae, J.-K. Park, and J. C. Ye, "Self-reference quantitative phase microscopy for microfluidic devices," Opt. Lett. **35**(4), 514–516 (2010).
19. B. Kemper, A. Vollmer, C. E. Rommel, J. Schnekenburger, and G. von Bally, "Simplified approach for quantitative digital holographic phase contrast imaging of living cells," J. Biomed. Opt. **16**(2), 026014 (2011).
20. N. T. Shaked, "Quantitative phase microscopy of biological samples using a portable interferometer," Opt. Lett. **37**(11), 2016–2018 (2012).
21. N. T. Shaked, T. M. Newpher, M. D. Ehlers, and A. Wax, "Parallel on-axis holographic phase microscopy of biological cells and unicellular microorganism dynamics," Appl. Opt. **49**(15), 2872–2878 (2010).
22. G. Popescu, L. P. Deflores, J. C. Vaughan, K. Badizadegan, H. Iwai, R. R. Dasari, and M. S. Feld, "Fourier phase microscopy for investigation of biological structures and dynamics," Opt. Lett. **29**(21), 2503–2505 (2004).
23. L. Xue, J. Lai, S. Wang, and Z. Li, "Single-shot slightly-off-axis interferometry based Hilbert phase microscopy of red blood cells," Biomed. Opt. Express **2**(4), 987–995 (2011).
24. B. A. E. Saleh and M. C. Teich, "Fourier optics," in *Fundamentals of Photonics*, B. A. E. Saleh ed. (Wiley, 1991), pp. 102–149.
25. B. A. E. Saleh and M. C. Teich, "Statistical optics," in *Fundamentals of Photonics*, B. A. E. Saleh ed. (Wiley, 1991), pp. 403–442.
26. D. C. Ghiglia and M. D. Pritt, *Two-Dimensional Phase Unwrapping: Theory, Algorithms, and Software* (Wiley, 1998).
27. S. Reyntjens and R. Puers, "A review of focused ion beam applications in microsystem technology," J. Micromech. Microeng. **11**(4), 287–300 (2001).
28. Y. K. Park, M. Diez-Silva, G. Popescu, G. Lykotrafitis, W. Choi, M. S. Feld, and S. Suresh, "Refractive index maps and membrane dynamics of human red blood cells parasitized by Plasmodium falciparum," Proc. Natl. Acad. Sci. U.S.A. **105**(37), 13730–13735 (2008).
29. I. Shock, A. Barbul, P. Girshovitz, U. Nevo, R. Korenstein, and N. T. Shaked, "Optical phase nanoscopy in red blood cells using low-coherence spectroscopy," J. Biomed. Opt. **17**(10), 101509 (2012).
30. J. W. Goodman, "Coherence of optical waves," in *Statistical Optics*, B. A. E. Saleh ed. (Wiley, 2000), pp. 157–226.

1. Introduction

Wide-field interferometric phase microscopy (IPM), also known as digital holographic microscopy, is a label-free powerful tool that can be utilized for a wide range of applications including biological cell investigations [1–5], surface measurements [6], biometry [7], and others. When imaging transparent samples, IPM is able to capture the two-dimensional optical path delay (OPD) or optical thickness map of the sample and track sub-nanometric changes occurring in it, with acquisition frame rates of up to several thousands of full frames per second.

IPM uses interference to record the complex wave front (amplitude and phase) of the light interacted with the sample. For biological and medical applications, the ability to record the sample quantitative phase enables the user to see cells and organisms, which are otherwise transparent due to the low absorption and scattering of the light transmitted through the cells.

Many IPM setups were presented over the years, and they can be divided into various groups, such as setups that use common-path geometry [8–10] or separated reference and sample beam geometry [1,2,5,11], setups that use high-coherence source [1–7] or low-coherence source [12–14], setups that use on-axis (inline) geometry [11,15] or off-axis geometry [1,2,5,12–14,16–19], etc. Many of these interferometric setups, however, have the same main drawbacks of bulkiness, non-portability and the requirement for specific optical skills to align and use them. These shortcomings cause this technology to largely remain in optical research laboratories, and thus it is not very common in the industry or in clinics. However, due to the recent technological developments and system miniaturization

#178929 - $15.00 USD Received 1 Nov 2012; revised 24 Dec 2012; accepted 1 Jan 2013; published 1 Mar 2013

capabilities, this situation is expected to change rapidly, with the suggestion of portable and relatively inexpensive setups [8–11,15–20]. One of these setups is the τ interferometer that was proposed by us lately [20]. The advantage of this interferometric device is that it can be attached to the camera port of a conventional transmission microscope, while still obtaining high-quality interferograms of the samples without the need for special optical skills or complicated alignment prior to the experiment. This device is inexpensive and is built using simple optical elements. Since the light splits and merges only after the output of the microscope, while using spatial filtering to erase the information from one of the beams before it merges with the other beam, this setup can be considered as a common-path interferometer, and thus it is more stable compared to regular interferometers. In addition, this setup can be easily adjusted with a low-coherence light source, which creates clearer images with less coherent noise. In contrast to regular interferometers, since there is only one sample beam till the output of the inverted microscope, the user does not need to take into consideration the thickness of the constant sample elements such as the coverslip in order to create beam path matching for achieving interference with a low-coherence source. Due to these advantages, this setup achieved a low temporal and spatial noise levels, with standard deviations of 0.18 nm and 0.42 nm, respectively.

However, the τ interferometer is mainly built to operate in on-axis geometry, where there is no angle between the sample and the reference beams. On-axis geometry limits the acquisition of dynamic changes as more than a single exposure is needed to obtain the quantitative phase profile of the sample [21,22], while the sample might change between the frames of acquisition. In addition, complex elements, such as phase modulators, should be used to create the needed different exposures. As shown in Ref. [20], off-axis interference can still be obtained using the τ interferometer, at the edges of the on-axis interference pattern [23] but with a very limited field of view of approximately 50 microns with 40× magnification, which practically means that it is incapable of imaging an area containing more than several cells under this magnification.

In this paper, we propose the off-axis τ interferometer, an important modification to the previously suggested τ interferometer. The proposed setup can operate in full off-axis geometry, obtain interference on a large field of view (limited only by the coherence length of the source) and use the full frame rate of the camera, while still retaining the advantages of the device portability, low cost, and easy alignment, even with a low-coherence source.

2. Off-axis τ interferometer setup

The conventional τ interferometer setup is shown in Fig. 1(a). In this setup, the image plane in the output of the microscope is Fourier transformed by lens L1, while being split into two beams using a beam splitter. One of the beams (defined as the sample beam) is reflected by the mirror M1 and then Fourier transformed back to the camera plane using lens L2, whereas the other beam (defined as the reference beam) is spatially filtered by pinhole P, reflected by mirror M2, and Fourier transformed back to the camera plane by lens L2. The spatial filtering effectively creates a reference beam by erasing the sample information from one of the beams, and thus enables quantitative interference on the camera. Using a pinhole in the reference beam path also increases the beam spatial coherence.

In this setup, the two beams are on the same optical axis, causing the beams to propagate in the same direction after L2 lens. This setup generates, in principle, an on-axis interference pattern on the digital camera, which reduces the dynamic capabilities of this setup, since in this case several phase-shifted interferograms are required for the reconstruction process.

To reconstruct the sample profile using one interferogram, one can shift the camera to the edge of the interference pattern so that an off-axis interferogram appears on a small area where the fringes are parallel straight lines. However, this can be obtained in a very limited field of view, and thus the sample size that can be recorded is significantly reduced.

#178929 - $15.00 USD Received 1 Nov 2012; revised 24 Dec 2012; accepted 1 Jan 2013; published 1 Mar 2013

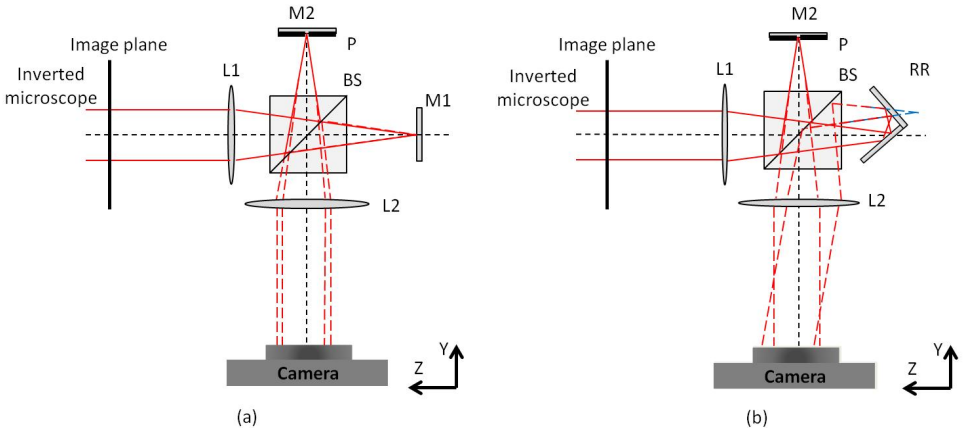

Fig. 1. Schematic system diagrams of: (a) the conventional τ interferometer [20]; (b) the off-axis τ interferometer. L1,L2 – lenses in a 4f configuration, BS – beam splitter, M1,M2 – mirrors, P – pinhole, RR – retro-reflector made of a two-mirror construction.

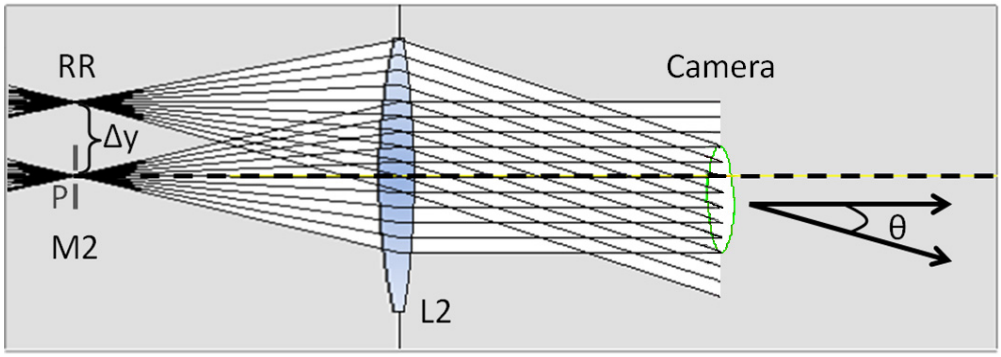

Fig. 2. Explanation for the retro-reflector (RR) operation using ray tracing of the sample and the reference beams in the off-axis τ interferometer, as it would be seen if they were on the same optical axis.

To solve these problems, we propose a new setup, which is an important modification of the previously proposed τ interferometer. Figure 1(b) presents the newly proposed off-axis τ interferometer, which is able to create a full off-axis interference pattern on the camera. In order to create an angle between the sample beam and the reference beam, and enable an off-axis interferogram, the actual Fourier plane center, described by the continuation of the reflected beam (blue lines in Fig. 1(b)), is shifted using retro-reflector RR. This retro-reflector is built using a pair of mirrors attached to each other in a right angle.

To explain the operation of the retro-reflector in the off-axis τ interferometer, Fig. 2 shows the two beam ray tracing as it would be seen if they both were on the same optical axis (so that a beam splitter was not used inside the 4f system composed of lens L1 and L2, but still the splitting would be imaginably performed). As can be seen from this figure, the retro-reflector creates an angle θ between the beams, which is described as follows:

$$\theta = \arctan(\Delta y / f), \tag{1}$$

where Δy is the shift between the focal points of the two beams, and f is the focal length of lens L2.

#178929 - $15.00 USD Received 1 Nov 2012; revised 24 Dec 2012; accepted 1 Jan 2013; published 1 Mar 2013

To demonstrate the operation of the off-axis τ interferometer, we have constructed the experimental setup illustrated in Fig. 3. This setup contains an inverted microscope with a single 40×, 0.66-numerical-aperture, infinity-corrected microscope objective, a spherical tube lens with 15 cm focal length, and a monochromatic CMOS camera with 5.2 µm square pixels (DCC1545M, Thorlabs). The camera was set on the maximum exposure time possible without reaching saturation, gamma value of 1 and no gain. The off-axis τ interferometer described above is connected between the microscope camera port and the digital camera.

The light source used in the input of the invert microscope is a supercontinuum fiber-laser source (SC400-4, Fianium), connected to a computer-controlled acousto-optical tunable filter (SC–AOTF, Fianium), tuned to a central wavelength of 633 nm and a full-width-at-half-maximum bandwidth of 6.7 nm, as measured by a compact spectrometer (USB4000-VIS-NIR, Ocean Optics), leading to a coherence length of 26.4 µm. To collimate the beam in the output of the tunable filter and to increase its spatial coherence, the beam was spatially filtered using 10× and 5× microscope objectives and a 25-µm confocally-positioned pinhole, creating magnification of 0.5. Note that the condenser lens was removed from the inverted microscope so that we can compare the performance of the system with other conventional IPM setups which use plane-wave illumination (see Section 4). In spite of this, as confirmed experimentally, the proposed interferometric setup can also operate when the inverted microscope uses a condenser lens, while improving the spatial resolution of the microscope and better using the numerical aperture of the objective lens.

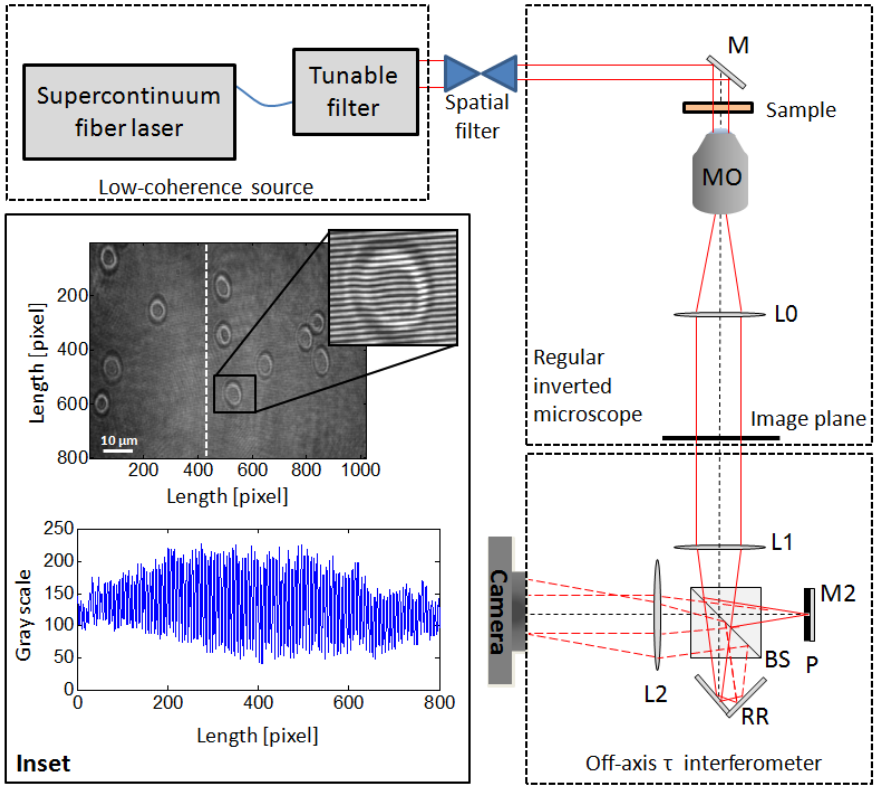

Fig. 3. The off-axis τ interferometer, connected in the output of an inverted microscope, which is illuminated by a tunable low-coherence source. MO – microscope objective, L0,L1,L2 – lenses, where L1 and L2 are in a 4f configuration, BS – beam splitter, M,M2 – mirrors, P – pinhole, RR – two-mirror retro-reflector. Inset: Wide-field off-axis interferogram of red blood cells obtained with the system, and its cross-section at the location indicated by the white line.

#178929 - $15.00 USD Received 1 Nov 2012; revised 24 Dec 2012; accepted 1 Jan 2013; published 1 Mar 2013

Lenses L1 and L2 were chosen to be achromatic lenses with focal lengths of 100 mm and 125 mm, respectively. The total magnification of the experimental setup was 47× and the experimentally confirmed diffraction-limited spot was 0.815 μm. The interference area on the camera sensor was 5.32 mm × 5.32 mm (1024 × 1024 pixels of 5.2 μm each) with a high-visibility modulation area (above half of the maximum visibility) of 2.672 mm × 5.32 mm (512 × 1024 pixels) and a fringe frequency of 48 lines per mm (fringe cycle of 4 pixels).

The inset in left bottom side of Fig. 3 shows the off-axis low-coherence interferogram of a sample containing live red blood cells obtained by the proposed system. A cross section along the white broken line is shown in this inset as well, to demonstrate the high fringe visibility obtained by the off-axis τ interferometer on a wide field of view containing several cells.

Based on the Fraunhofer diffraction through a circular aperture [24], the pinhole diameter in the off-axis τ interferometer is chosen to be 30 μm. This pinhole size ensures that most of the sample-image data is erased and that the first airy disk defined by the pinhole covers most of the camera sensor where the interference fringes appear [14]. We also checked the pinhole compliance with the Fraunhofer diffraction criterion using MATLAB simulation of low spatial frequency phase images.

In addition to its portability, simple, compact and inexpensive design, one of the greatest advantages of the off-axis τ interferometer is its simple alignment. Using this interferometer, obtaining interference with a high-coherence source, such as a HeNe laser, is immediate, and the alignment with a low-coherence source is significantly easier compared to obtaining low-coherence interference with conventional interferometers such as the Mach-Zehnder or the Michelson interferometers. The alignment of the off-axis τ interferometer using a low-coherence source is done by firstly aligning the pinhole on the combined focal point of lenses L1 and L2 and obtaining a circular diffraction image on the camera plane. It is assumed that the illumination is parallel to the microscope optical axis, or otherwise one needs to correct the illumination angle or shift the position of the pinhole. Following this, the retro-reflector is positioned in such a way that on both of its mirrors the beam spots have equal size, while both spots appear as close as possible to the connection between the two mirrors. By doing so, the OPD between the two beams will be close to obtaining an on-axis interference. Then, RR is shifted in z direction until an interference pattern between the beams is obtained on the camera. Following this, shifting RR in the y direction creates an off-axis interference pattern on the camera, with an angle determined by Eq. (1).

3. Data processing

The interferogram, created on the digital camera sensor using a low-coherence source, is described by the following expression [25]:

$$I = \left\langle |V_s + V_r|^2 \right\rangle = I_s + I_r + G_{+1} + G_{-1}. \quad (2)$$

where $\langle \bullet \rangle$ represents ensemble average, V_s and V_r are the sample and reference complex waves respectively, I_s and I_r are the intensities of sample and reference beams respectively, and G_{+1} and G_{-1} are the temporal coherence functions (G_{+1} and G_{-1} are complex conjugates) which, under high spatial coherence assumption, can be expressed as follows (see Appendix A):

$$G_{+1} = \sqrt{I_s I_r} \times \exp\left[-\frac{|OPD_{total}|}{l_c(x,y)} \right] \times \exp\left[-j\frac{2\pi}{\lambda} OPD_{total} \right] \times \exp\left[-j\frac{2\pi}{\lambda} y \sin(\theta) \right], \quad (3)$$

where OPD_{total} is the spatially-varying total OPD (including the sample and its surrounding immersion medium), $l_c(x,y)$ is the coherence length projected on the axis perpendicular to the camera plane, and λ is the mean illumination wavelength (assuming linear off-axis fringes across the y axis).

#178929 - $15.00 USD Received 1 Nov 2012; revised 24 Dec 2012; accepted 1 Jan 2013; published 1 Mar 2013

The digital extraction of the sample phase from the off-axis interferogram is carried out by digital spatial filtering, which includes a digital two-dimensional Fourier transform, separation of the temporal coherence function G_{+1} from the zero-order $I_s + I_r$, and back Fourier transform of the centered temporal coherence function G_{+1}. Then, we take the phase argument of the resulting complex function to obtain the wrapped phase. To compensate for aberrations and field curvatures, we perform the same wrapped-phase extraction process for a sample-free interferogram, and the result is subtracted from the first wrapped phase by dividing the sample complex wavefront with sample-free complex wavefront. Finally we apply a quality-guided two-dimensional unwrapping algorithm to remove 2π ambiguities, yielding the unwrapped phase profile which is equal to $(2\pi/\lambda)\times OPD_{total}$ [26].

Under the assumption of a constant chamber thickness and a constant immersion medium refractive index n_m around the sample, the OPD profile of the sample (OPD_s) can be extracted from OPD_{total} by subtracting all the elements having a constant refractive index and thickness (see Appendix A, Eq. (A3), and written as follows [2,5]:

$$OPD_s(x,y) = [\bar{n}_s(x,y) - n_m] \times h_s(x,y), \tag{4}$$

where h_s is the thickness profile of the sample and $\bar{n}_s$ is the sample integral refractive index, which is defined as follows [2,5]:

$$\bar{n}_s(x,y) = \frac{1}{h_s(x,y)} \int_0^{h_s(x,y)} n_s(x,y,z)dz. \tag{5}$$

4. Experimental results

4.1 Measuring the spatial and temporal OPD sensitivities of the system

First, to estimate the setup spatial and temporal noise levels, which determine the OPD sensitivity across an image and between images, respectively, we recorded two different samples, a plain coverslip and a chamber containing only water. For this experiment, we continuously recorded 150 interferograms of 512 × 512 camera pixels during 10 seconds, and processed them to the coinciding OPD maps, as explained above. Figure 4(a) presents the standard deviation distribution of the 150 OPD maps containing 512 × 512 pixels for the dry sample (each value is from a different OPD map). This distribution represents the spatial stability of the system indicating on the spatial noise in the OPD maps. As can be seen from Fig. 4(a), most of the values are around 0.6 nm. In the center of the image (a central area of 150 × 150 pixels), where the visibility is higher than 0.75, the spatial stability value was only

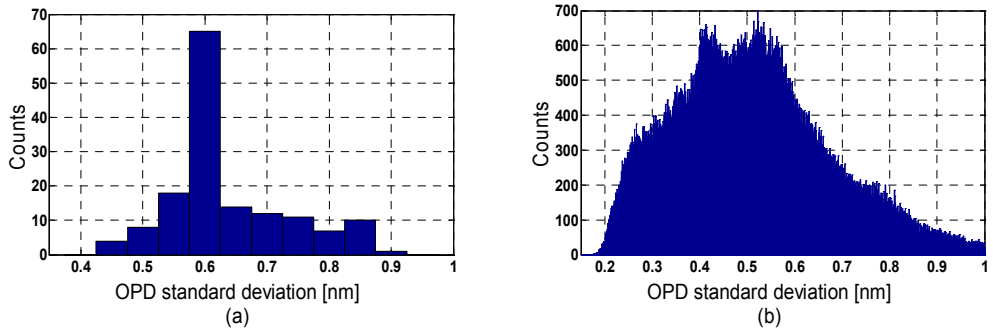

Fig. 4. OPD sensitivities in a dry sample: (a) Spatial sensitivity: OPD standard deviation across a single OPD map for each of the 150 OPD maps. (b) Temporal sensitivity: OPD standard deviation for each diffraction-limited spot across the 150 OPD maps.

#178929 - $15.00 USD Received 1 Nov 2012; revised 24 Dec 2012; accepted 1 Jan 2013; published 1 Mar 2013

0.35 nm. Figure 4(b) shows the standard deviation distribution per a single diffraction-limited spot across the 150 OPD maps for the dry sample, representing the temporal stability of the system. The mean temporal stability measured was 0.5 nm, where in the center of the image it was 0.24 nm. For the wet sample, the temporal stability had an average value of 0.54 nm, whereas in the center of the image it was only 0.28 nm.

4.2 Volume holographic grating measurements

To assess the capabilities of the off-axis τ interferometer, measurements on several targets were performed and compared with these obtained by an off-axis Mach-Zehnder interferometer, a common IPM setup [5], when using both a high-coherence source (HeNe laser) and a low-coherence source with a spectral bandwidth of 6.7 nm. We now present comparative results between the systems under the exact same conditions (where the systems operated using the same low-coherence light source, camera, optical table, etc.) The same fringe visibility area was chosen and the same reconstruction algorithm was applied in all cases.

The first measured sample was a new 600 lp/mm volume phase holographic grating (from Edmunds Optics). This grating is characterized by a constant physical thickness and a periodic refractive index profile with a constant amplitude and frequency. Figure 5 presents the measurements done on the center of the grating using both the off-axis τ interferometer and the off-axis Mach-Zehnder interferometer, both using the same low-coherence source. By comparing the results of both setups, it can be seen that both setups managed to recognize the periodic refractive index profile of the grating. However, the off-axis τ interferometer provided a significantly clearer and more consistent image (see Fig. 5(a)) compared to the conventional off-axis Mach-Zehnder interferometer (see Fig. 5(b)), which yielded artifacts such as brakes in the ridges and inconstant base plane.

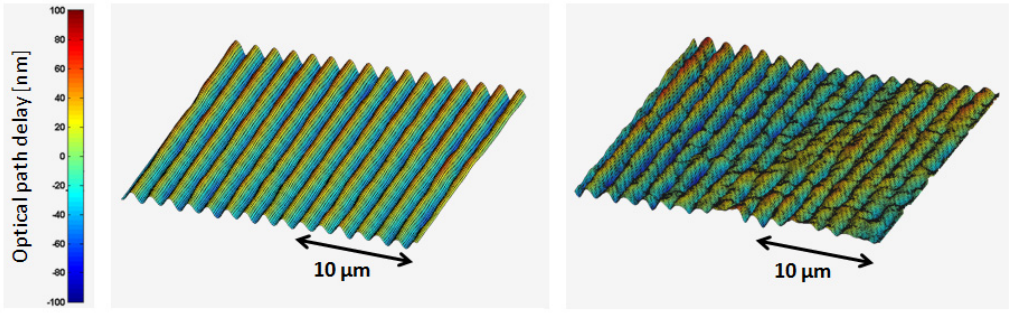

Fig. 5. OPD maps of a volume phase holographic grating obtained under low-coherence illumination by: (a) the off-axis τ interferometer; and (b) the off-axis Mach-Zehnder interferometer.

4.3 Measurements of custom-made phase targets

Two other phase targets were designed in the computer and then generated by focused ion beam (FIB) lithography. FIB lithography operates in a similar fashion of a scanning electron microscope (SEM) but rather uses a finely focused gallium beam. FIB is capable of milling the surfaces of substrates and creating nanometer-scale-topography phase targets [27].

Using FIB lithography, we created several shapes on a chrome-plated glass coverslip (10 nm plating) in different heights, ranging from 10 nm to 300 nm. The first element was a large plate-like shape with a curvature inside, with our university logo in the middle of the plate lithographed with a deeper milling. Six smaller plate-like shapes were lithographed

#178929 - $15.00 USD Received 1 Nov 2012; revised 24 Dec 2012; accepted 1 Jan 2013; published 1 Mar 2013

symmetrically inside the large plate with deeper curvatures. To better explain the shapes lithographed on the glass coverslip, an SEM image of a similar element made on a silicon substrate from the same computer model is shown in Fig. 6.

Figure 7 presents the OPD map of this new phase target as obtained by the off-axis τ interferometer using a low-coherence source (Fig. 7(a)), by the off-axis Mach-Zehnder interferometer using a low-coherence source (Fig. 7(b)), and by the Mach-Zehnder interferometer using a high-coherence source (Fig. 7(c)). While the three configurations managed to record the logo in the center of the plate, the off-axis Mach-Zehnder interferometer failed in recording the large plate curvature, as well as could hardly visualized the smaller six plates around the logo, due to higher spatial noise level. In Fig. 7(c), the effects of the coherent noise and the self interferences of the high-coherence source distorted the thinnest elements, i.e. the six small plates and larger plate.

The second phase target, lithographed by the same FIB technique, contained the words "OMNI Group" with a line width of 0.7 μm (close to the microscope diffraction-limit spot) and an optical thickness of 20 nm (10 nm due to the milling of the chrome and 10 nm due to the milling of the glass). Again, we compared three cases: the off-axis τ interferometer using a low-coherence source, an off-axis Mach-Zehnder interferometer using a low-coherence source, and an off-axis Mach-Zehnder interferometer using a high-coherence source.

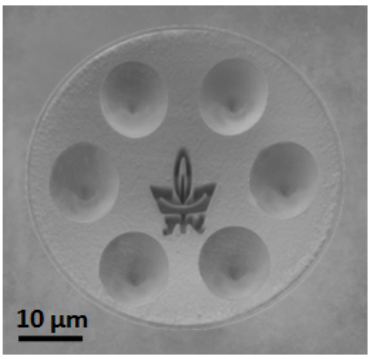

Fig. 6. SEM image of an element similar to our first lithographed phase target.

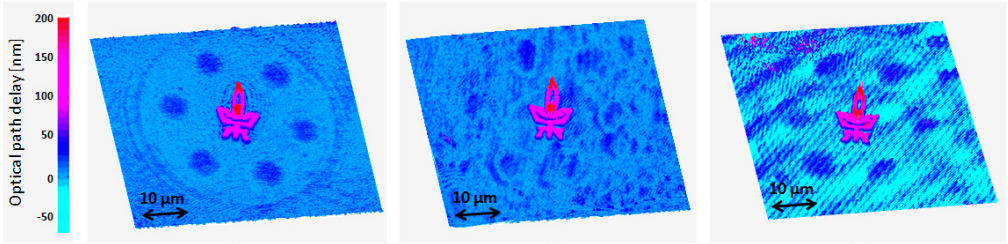

Fig. 7. OPD maps of the first phase target created by FIB lithography, containing variable depths elements (see Fig. 6), as obtained using: (a) the off-axis τ interferometer with a low-coherence source; (b) the off-axis Mach-Zehnder interferometer with a low-coherence source; and (c) the off-axis Mach-Zehnder interferometer with a high-coherence source (HeNe laser).

#178929 - $15.00 USD Received 1 Nov 2012; revised 24 Dec 2012; accepted 1 Jan 2013; published 1 Mar 2013

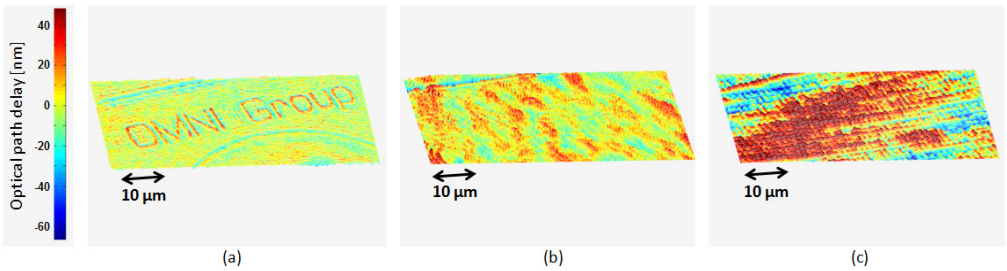

Fig. 8. OPD maps of the second phase target created by FIB lithography, containing variable depth elements, as obtained using: (a) the off-axis τ interferometer with a low-coherence source; (b) the off-axis Mach-Zehnder interferometer with a low-coherence source; and (c) the off-axis Mach-Zehnder interferometer with a high-coherence source (HeNe laser).

The corresponding OPD maps are shown in Figs. 8(a-c). As it was for previous target, the lower spatial noise level of the off-axis τ interferometer enables it to see smaller features that the other conventional IPM setups cannot see. In Fig. 8(a), the lithographed text "OMNI Group" is clearly seen and distinguished from the background, whereas in the measurements done by the off-axis Mach-Zehnder interferometer, presented in Figs. 8(b,c), the background noise level conceals most of the lithographed text and only several lines are barely seen.

The mean OPD of the lithographed text letters in Fig. 8(a) is measured as 20 nm, which agrees with the real OPD of the letters that was calculated as 19.4 nm ($n_{\text{chrome}} = 2.42$ and $n_{\text{glass}} = 1.515$). Note that minimal milling capability of the FIB setups used by us is 10 nm, so it is possible that the inconstant OPD of the letters seen in Fig. 8(a) is caused by the milling process of the glass layer and not due to the spatial interferometric noise. In any case, these results show that the off-axis τ interferometer can be used to perform inexpensive quality checks and imaging during or after the manufacturing of transparent optical elements, as long as the lateral dimensions of the smallest element that needs to be examined is larger than the diffraction-limit spot of the microscope.

4.4 Biological cell dynamic measurements

We next measured red blood cell (RBC) membrane fluctuations, where we captured 300 OPD profiles at 25 frames per second. Figure 9 shows the OPD and the physical thickness profile of RBC samples from both setups while using a low-coherence source (Figs. 9(a) and 9(b), respectively), and the corresponding temporal standard deviation maps (Figs. 9(c) and 9(d), respectively). The color bar in Fig. 9 shows both the OPD values and the physical thickness values based on refractive indices assumptions of 1.395 for the RBCs and 1.33 for the surrounding medium [28].

The OPD profiles show a slightly lower spatial noise level in the off-axis τ interferometer (comparing Figs. 9(a) and 9(b), with more self-interferences in the bottom right side of Fig. 9(b)). Note that none of the images have been digitally treated to improve its quality. The standard deviation calculated from using the Mach-Zehnder interferometer showed higher temporal noise levels with a mean background value of 1.1 nm, compared to only 0.32 nm in the off-axis τ interferometer (see Figs. 9(c,d)). The standard deviations of the RBC OPD fluctuations were similar for the two types of measurements, ranging from 0.7 nm to 7 nm [29]. Note that not all membrane fluctuations were seen using the Mach-Zehnder interferometer, as in some cases the temporal noise level was higher than the lowest measurable OPD standard deviation.

One of the advantages of the off-axis τ interferometer, in contrast to the conventional τ interferometer [20], is the capability of recoding dynamic changes in a larger field of view, where the frame rate is limited only by the maximal frame rate of the camera sensor (since

#178929 - $15.00 USD Received 1 Nov 2012; revised 24 Dec 2012; accepted 1 Jan 2013; published 1 Mar 2013

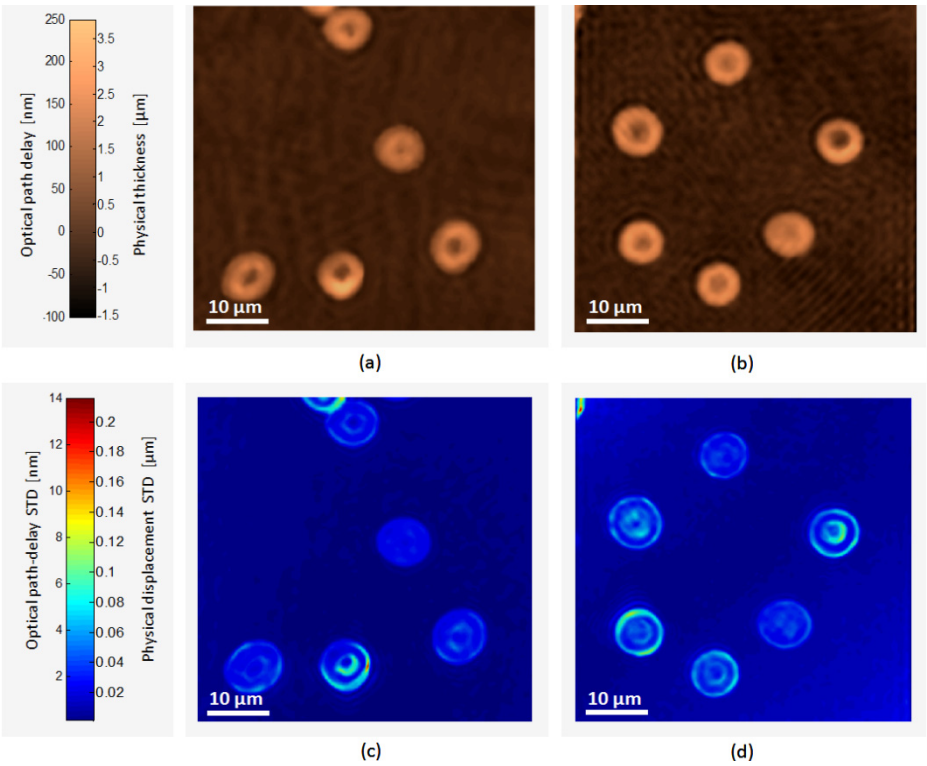

Fig. 9. OPD and physical thickness maps of RBCs, obtained using a low-coherence source in: (a) the off-axis τ interferometer; and (b) the off-axis Mach-Zehnder interferometer. The standard deviation of the OPD and of the physical thickness maps for: (c) the off-axis τ interferometer; and (d) the off-axis Mach-Zehnder interferometer.

only one frame of acquisition is required to reconstruct the OPD map). To emphasize the importance of this capability, we also recorded Blepharisma organism in motion, as it swims through the entire field of view. Blepharisma is a red-colored single-cell microorganism found in fresh or salt water. It has external cellular organelles that are used for movement and food gathering.

Figure 10 and Media 1 present the Blepharisma organism swimming in water at a frame rate of 25 frames per second. The entire motion across the field of view lasted less than half a second, where there is not a point in time where the Blepharisma was stationery. This recording cannot be done with the τ interferometer in the on-axis configuration using the same frame rate of the camera, since more than a single frame of acquisition is needed to retrieve the OPD map.

As can be seen in Fig. 10 and Media 1, at 0 msec, 40 msec, 320 msec and at 360 msec, due to the low-coherence length of the light source, the reconstruction of the Blepharisma image is not complete. In the first two cases (0 and 40 msec), the lower coherence length causes a low visibility of the interference fringes in some areas at the edges of the frame. In these areas, the interference visibility is low and the phase cannot be well reconstructed. In the last two cases (320 and 360 msec), the Blepharisma is positioned in an angle to the imaging plane, which causes an erroneous reconstruction in these out-of-focus points, so not all parts of the organism are reconstructed correctly. The first problem can be solved by using a coherent source as the coherence length will increase; however, coherent noise will be higher while decreasing the system sensitivity [14].

#178929 - $15.00 USD Received 1 Nov 2012; revised 24 Dec 2012; accepted 1 Jan 2013; published 1 Mar 2013

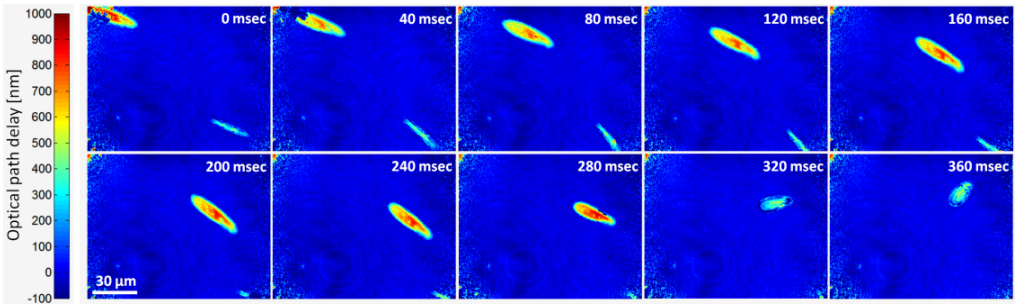

Fig. 10. Measurements of Blepharisma organism swimming in water using the off-axis τ interferometer, demonstrating the system capabilities for quantitative imaging of fast dynamics on relatively large field of view due to its true off-axis configuration, and as opposed to the conventional τ interferometer [20]. See video in Media 1.

5. Discussion and conclusions

In addition to the facts that the proposed interferometer is smaller, less expensive, more portable and significantly easier to construct and to align compared to the conventional off-axis IPM setups, the results presented in this paper show that the off-axis τ interferometer provides higher quality and clearer OPD maps, with lower spatial and temporal noises.

The proposed interferometer is able to record a single interferogram containing more than 1 Mega pixels (an area of 5.32 mm × 5.32 mm on our camera sensor), and due to its off-axis geometry, it allows multi-cell imaging in a single frame of acquisition, as opposed to the previously proposed τ interferometer [20].

The temporal and spatial noises, determining the smallest temporal and spatial OPD change that can be detected by the setup, are in the sub-nanometer range with values of less than 0.7 nm for the full image and less than 0.4 nm in the center of the image. Further improvement may be obtained by tilting the field in one of the beams using diffraction grating to create a full-field, high-visibility interference on the entire camera plane [14].

In contrast to the off-axis τ interferometer, a conventional off-axis Mach-Zehnder interferometer with a low-coherence light source failed to record the clear phase profile of the phase grating used as a test target, though the experimental environments were identical in both cases. In case of the Mach-Zehnder interferometer, since the two waves creating the interference pattern propagate through different physical paths with different optical elements (mirrors, lenses, beam splitters, etc.), the two waves acquire different spatial noises, which leads to reduction in the light coherence and to distortion of the reconstructed sample OPD profile, as opposed to the proposed τ interferometer. In the conventional off-axis Mach-Zehnder interferometer used for IPM, there might be up to nine different optical elements in the interferometric beam paths, after the beams are split and before they are combined again (two beam splitters, two mirrors, two retro-reflectors, two objectives, and a sample stage), whereas in the proposed off-axis τ interferometer, there are only three elements in the interferometric beam paths (one beam splitter, one pinhole mirror and one retro-reflector).

One additional feature of the off-axis τ interferometer is that the phase of the wave reflected from the pinhole still contains the DC frequency of the original wave, caused by all parts of the sample with constant or very slowly varying optical thickness (such as the coverslip). Therefore, in our case the total OPD in the first and second exponent numerators of Eq. (3) should lack these constant thickness values. This increases the fringes visibility, reduces noise, and more importantly, prevents changes in the interference area due to using different coverslip thicknesses.

The off-axis τ interferometer managed to record FIB-lithographed elements with ~20 nm optical thickness, which otherwise would be obscured by the spatial noise, as well as

#178929 - $15.00 USD Received 1 Nov 2012; revised 24 Dec 2012; accepted 1 Jan 2013; published 1 Mar 2013

managed to detect dynamic cell thickness changes of 7 nm, with a relatively wide field of view, limited only by the coherence length of the source.

We expect that in mass production, the off-axis τ interferometer size can be reduced to a cube of 1 inch length, with total cost of less than $500. Due to its low cost and simple design and operation, we expect that this portable off-axis interferometer will make wide-field IPM measurements more common for clinical diagnosis, for biological research and for nondestructive testing in the industry, especially for users without optical skills and with limited resources.

Appendix A

Under high spatial coherence assumption, the complex degree of coherence can be expressed by the temporal coherence function (TCF) of the two interfering plane waves. In the case that there is no angle between the waves, the TCF can be expressed by the following expression [30]:

$$G_{+1} = \langle V_s^*(t) \times V_r(t+\tau) \rangle = \sqrt{I_s I_r} \times \exp\left[-\frac{|\tau|}{\tau_c} \right] \times \exp\left[-j2\pi \frac{c}{\lambda} \tau \right], \tag{A1}$$

where $\langle \bullet \rangle$ represents ensemble time average [25], V_s and V_r are the sample and reference complex waves respectively, I_s and I_r are the intensities of sample and reference beams respectively, c is the speed of light, τ_c is the coherence time, and τ is the time difference between the two waves, which can be calculated as follows:

$$\begin{aligned} t_1 = \frac{d}{c};\ t_2 = \frac{1}{c}\{[d - h_m(x,y)] + [h_m(x,y) - h_s(x,y)] \times n_m(x,y) + h_s(x,y) \times \overline{n}_s(x,y)\}; \\ \tau = t_2 - t_1 = \frac{1}{c}\{h_s(x,y) \times [\overline{n}_s(x,y) - n_m(x,y)] + h_m(x,y) \times [n_m(x,y) - 1]\}, \end{aligned} \tag{A2}$$

where t_1 and t_2 are, respectively, the time periods that the reference beam and the sample beam pass until interfering with each other, d is the total beam path (including propagation through air), $h_m(x,y)$ is the spatially-varying thickness of the medium surrounding the sample including the sample, $n_m(x,y)$ is the spatially-varying integral refractive index of the immersion media surrounding the sample (for example growth medium for biological cells *in vitro*), $h_s(x,y)$ is the spatially-varying thickness of the sample, and $\overline{n}_s(x,y)$ is the spatially-varying integral refractive index of the sample. Figure 11 presents a schematics explaining of the meaning of these variables. The total OPD can be written as follows:

$$\begin{aligned} OPD_{total}(x,y) &= c \cdot \tau \\ &= h_s(x,y) \times [\overline{n}_s(x,y) - n_m(x,y)] + h_m(x,y) \times [n_m(x,y) - 1] \\ &= OPD_s + OPD_m, \end{aligned} \tag{A3}$$

where $OPD_s = h_s(x,y) \times [\overline{n}_s(x,y) - n_m(x,y)]$ and $OPD_m = h_m(x,y) \times [n_m(x,y) - 1]$.

Using Eq. (A3), the TCF can be rewritten as follows:

$$\begin{aligned} G_{+1} &= \sqrt{I_s I_r} \times \exp\left[-\left| \frac{OPD_{total}}{c} \right| \frac{c}{l_c} \right] \times \exp\left[-j2\pi \frac{c}{\lambda} \frac{OPD_{total}}{c} \right] \\ &= \sqrt{I_s I_r} \times \exp\left[-\left| \frac{OPD_{total}}{l_c} \right| \right] \times \exp\left[-j \frac{2\pi}{\lambda} OPD_{total} \right]. \end{aligned} \tag{A4}$$

where l_c is the coherence length.

#178929 - $15.00 USD Received 1 Nov 2012; revised 24 Dec 2012; accepted 1 Jan 2013; published 1 Mar 2013

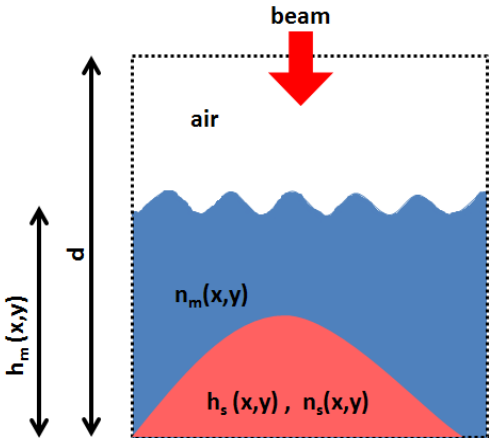

Fig. 11. Schematics of the sample and immersion medium thicknesses and refractive indices.

In case that there is an angle between the two interfering waves, Eq. (A4) can be rewritten as follows [24]:

$$G_{+1} = \sqrt{I_r I_s}\,\exp\left[-\frac{|OPD_{total}|}{l_c(x,y)}\right]\times\exp\left[-j\,\frac{2\pi}{\lambda}OPD_{total}\right]\times\exp\left[-j\,\frac{2\pi}{\lambda}y\,\sin(\theta)\right], \quad \text{(A5)}$$

where the third exponent represents the linear fringes of the interference (assuming an off-axis fringe pattern with straight parallel fringes across the y axis). Due to the angle between the waves, the coherence length projection on the perpendicular axis to the camera plane $l_c(x,y)$ depends on the position (x, y) [14].

Acknowledgments

Supported by the Israel Science Foundation (ISF) Bikura Grant and by the Marie Curie Career Integration Grant (CIG). We thank Haniel Gabai, Nir Turko and Irena Frenklach from the OMNI group for helpful discussions.

#178929 - $15.00 USD Received 1 Nov 2012; revised 24 Dec 2012; accepted 1 Jan 2013; published 1 Mar 2013